# Supporting Information

## Influence of halide choice on formation of low-dimensional perovskite interlayer in efficient perovskite solar cells

*Xueping Liu[‡], Thomas Webb[‡], Linjie Dai, Kangyu Ji, Joel A. Smith, Rachel C. Kilbride, Mozhgan Yavari, Jinxin Bi, Aobo Ren, Yuanyuan Huang, Zhuo Wang, Yonglong Shen, Guosheng Shao*, Stephen J. Sweeney, Steven Hinder, Hui Li, David G. Lidzey, Samuel D. Stranks, Neil C. Greenham, S. Ravi P. Silva*, Wei Zhang**

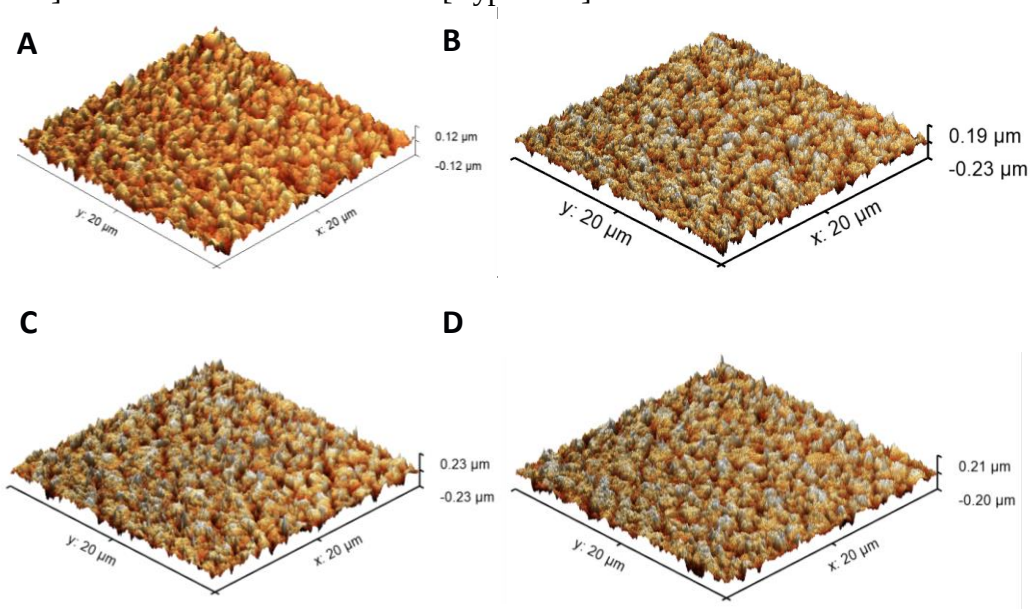


**Figure S1.** Atomic force microscopy images of control (A), neoPAI- (B), neoPABr- (C) and neoPACl-passivated (D) perovskite films.

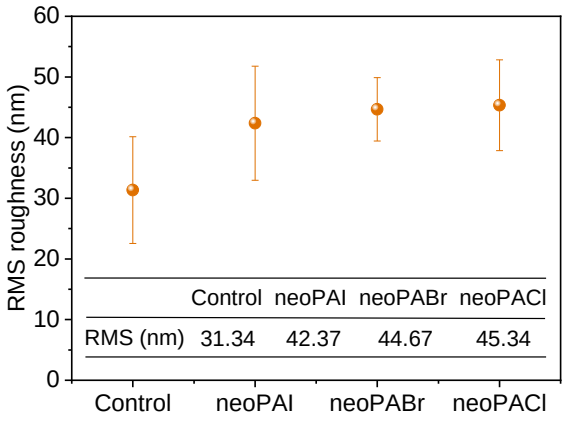


**Figure S2.** Calculated RMS roughness from AFM images of control and neoPAX passivated perovskite films.

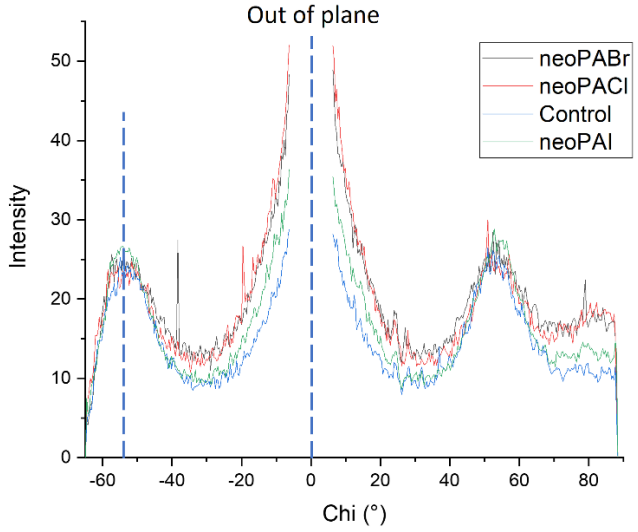


**Figure S3.** Perovskite (100) azimuthal intensity profile. The distribution of X-ray scattering for this plane exhibits the dominant orientation is <100> (100 out of plane), the secondary orientation at 54° corresponds to <111> orientation (this is confirmed by the higher intensity out of plane scattering in the (111) ring visible in the 2D images). Perovskite is slightly more <100> oriented after treatment by neoPACl and neoPABr.

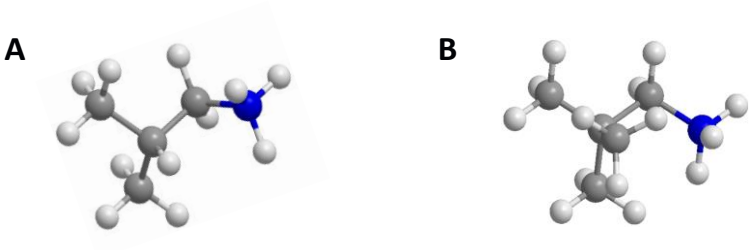


**Figure S4.** Diagram of the molecule of isoBA (A) with a chemical formula of $CH(CH_3)_2CH_2NH_3^-$ and neoPA (B) with a chemical formula of $C(CH_3)_3CH_2NH_3^-$.

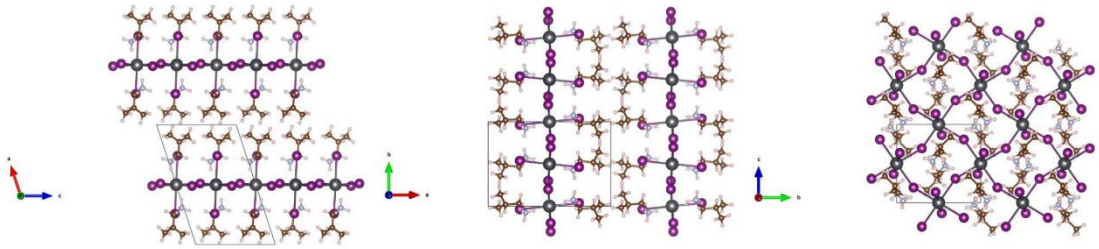

**Figure S5.** Diagram of $(isoBA)_2PbI_4$ structure from reference.[1]

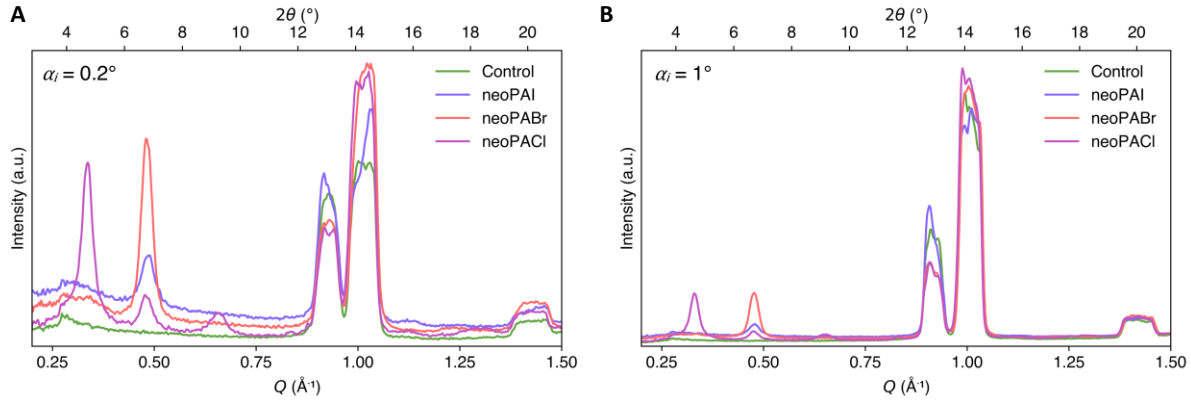


**Figure S6.** Azimuthally integrated GIWAXS patterns of neat and neoPAX-treated FA(MA)$PbI_3$ films at grazing incidence angles of (A) $\alpha_i$ = 0.2° and (B) $\alpha_i$ = 1°. X-ray attenutation lengths into the film surface were calculated assuming pure cubic $FAPbI_3$ with density 4.101 g $cm^{-3}$.[2] These are 242 nm at $\alpha_i$ = 1° and 495 nm at $\alpha_i$ = 2° (scattering data shown in Figure 2),[3] with 0.2° chosen to be close to the critical angle.

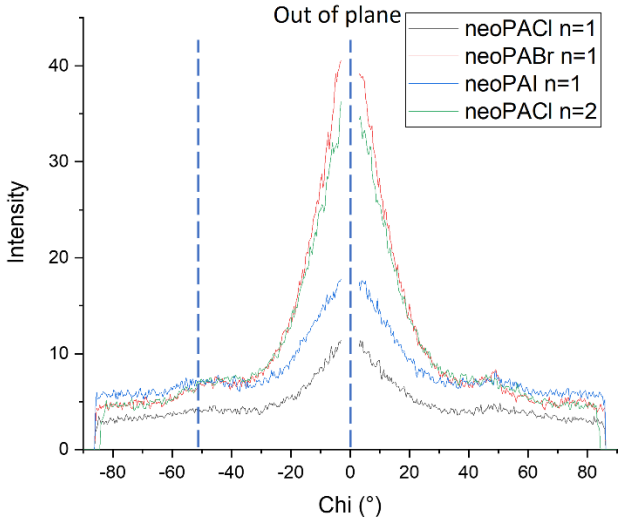


**Figure S7.** $N$ = 1 (100) and $n$ = 2 (020) azimuthal intensity profile. Both $n$ = 1 and $n$ = 2 phases form with parallel textured layers (out of plane scattering). Additional less defined orientation suggests that these phases also form on the perovskite (111) surface but preferentially grow on the (100) surfaces.

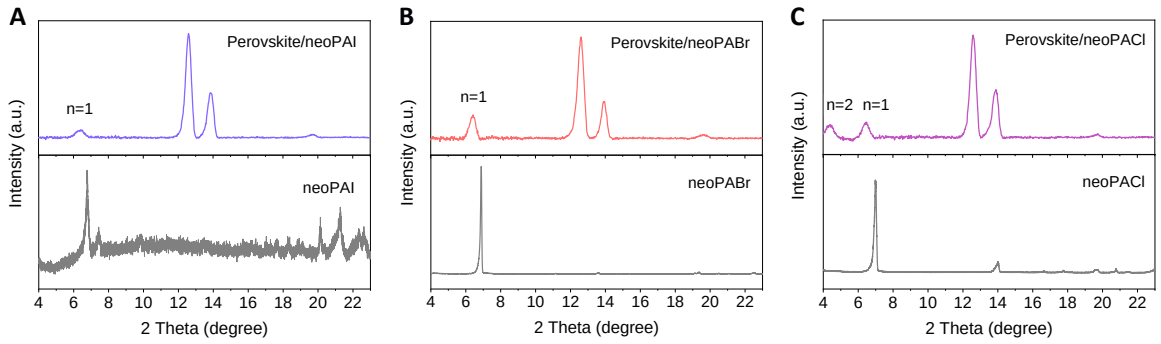


**Figure S8.** Comparison of grazing incidence X-ray diffraction (GIXRD) patterns of perovskite films passivated with neoPAI (A), neoPABr (B) and neoPACl (C) and corresponding neoPAX powders.

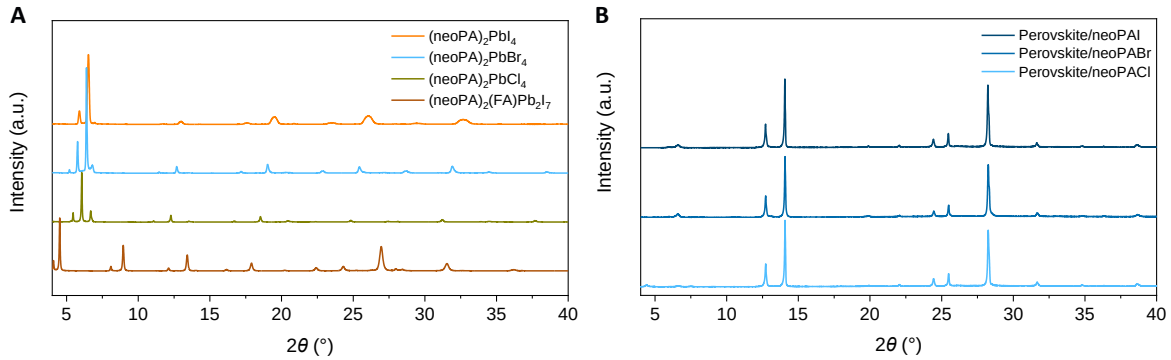


**Figure S9.** (A) Full XRD patterns from thin films of $(neoPA)_2PbI_4$, $(neoPA)_2PbBr_4$, $(neoPA)_2PbCl_4$ and $(neoPA)_2(FA)Pb_2I_7$. (see detail in Experimental Section). In each pattern, additional reflections are observed, consistent with a second phase with larger interplanar spacing. These are attributed to the films retaining some proportion of a high temperature phase introduced during the thermal annealing step, as has been reported for Ruddlesden-Popper phases.[4] (B) XRD patterns of 50 mM neoPAX/IPA solution treated perovskite films.

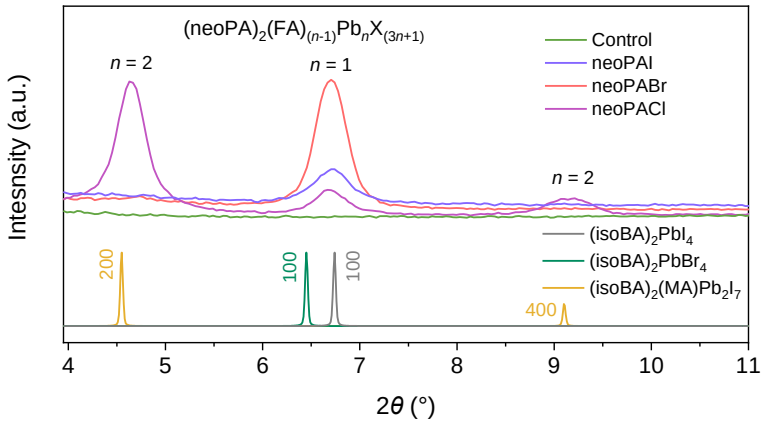


**Figure S10.** The highlighted low-angle region of $(neoPA)_2(FA)_{(n\text{-}1)}Pb_nX_{(3n+1)}$ Ruddlesden-Popper phases compared to simulated X-ray diffraction patterns from reported isobutylammonium lead halide phases, based on structural data given in references 3 and 6.[1, 5]

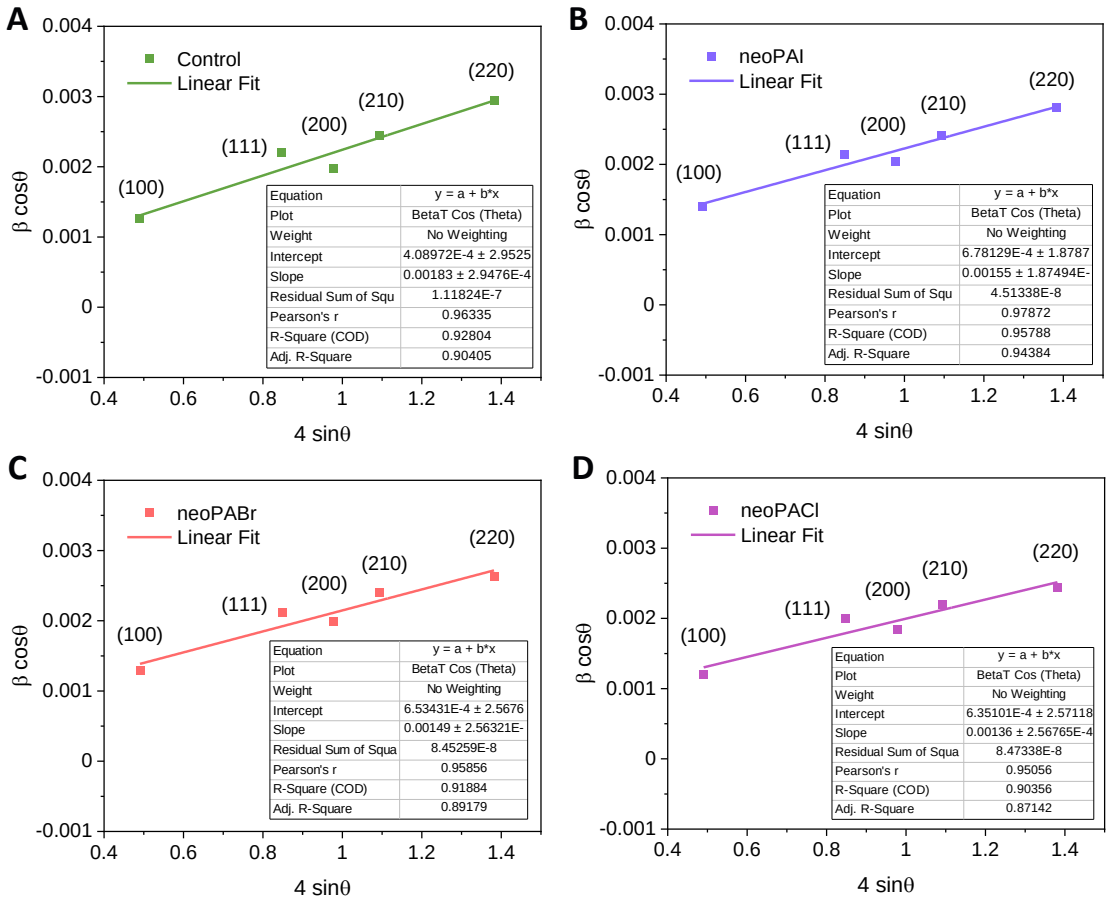


**Figure S11.** Williamson–Hall plots and corresponding parameter sheets for control films and the different alkylammonium halide treated samples. The lattice strain ($\varepsilon$) was calculated by the Williamson–Hall equation[6]:

$$\beta cos\theta = \left(\frac{K\lambda}{L}\right) + 4\varepsilon sin\theta$$

where $K$ is the sharp factor ($K$ = 0.94), $\lambda$ is the X-ray wavelength of Cu$K_\beta$ ($\lambda$ = 0.13847 nm), $L$ is the average crystallite size in nanometers, and $\theta$ is the Bragg angle in radian. Therefore, the lattice strain ($\varepsilon$) could be calculated from the slope of the liner curve when When $\beta$cos$\theta$ is the y-axis and 4sin$\theta$ is the x-axis.

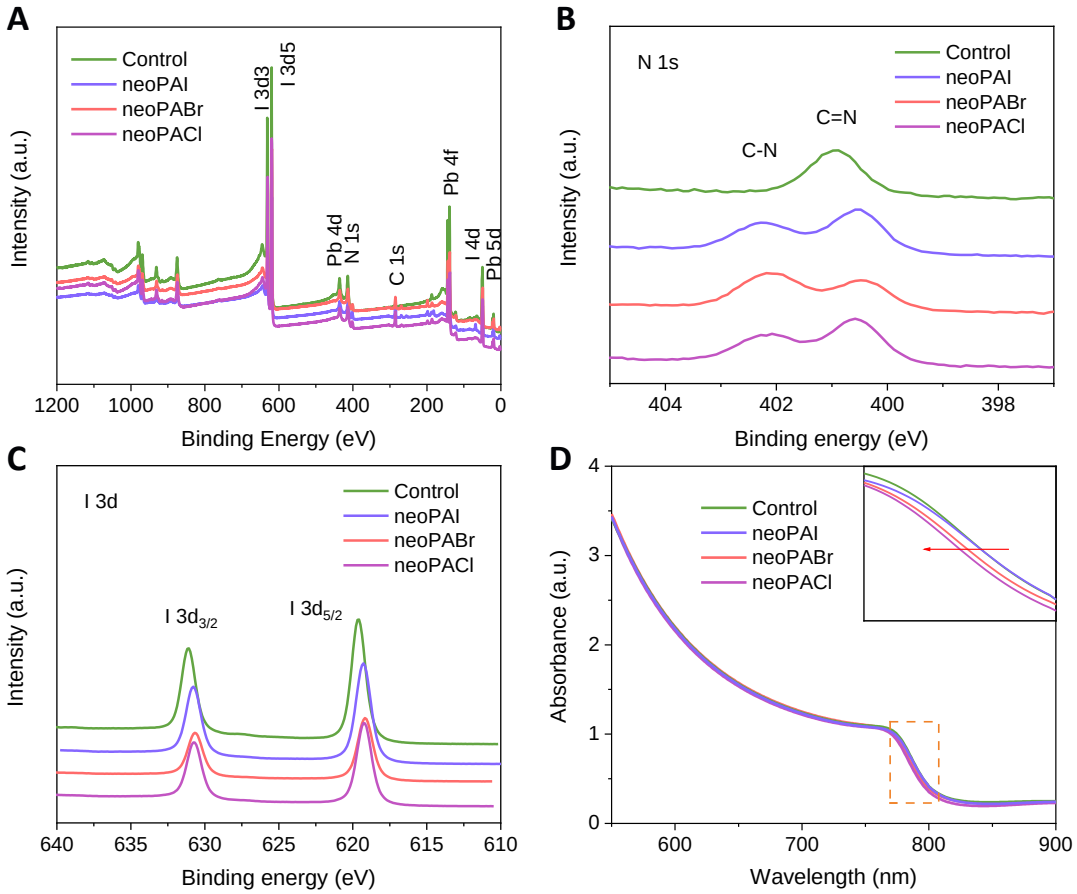


**Figure S12.** (A) XPS full scan spectra of the perovskite films without and with neoPAI, neoPABr and neoPACl passivation. High-resolution N 1s (B) and I 3d (C) core level spectra of perovskite films without and with the passivation of neoPAI, neoPABr and neoPACl. (D) UV–vis absorption spectra of the perovskite films (inset is an enlargement of the dashed region).

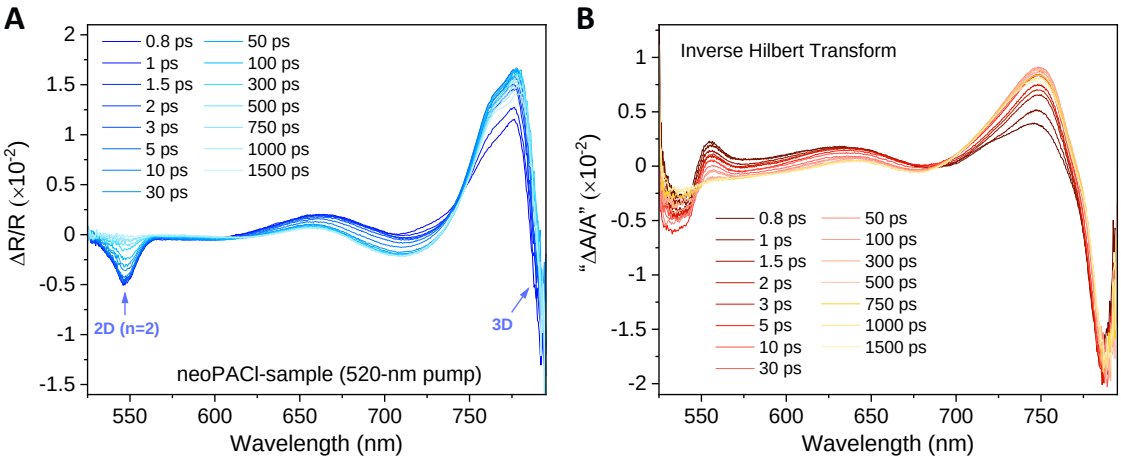


**Figure S13.** (A) Transient reflection spectra of neoPACl-passivated sample under a 520-nm pump, and (B) the corresponding inverse Hilbert transform of the TR spectra.

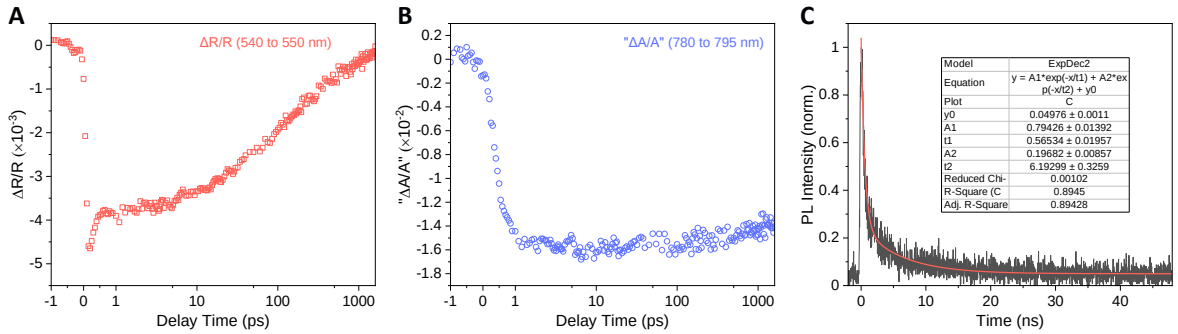


**Figure S14.** (A) The kinetics of the high-energy feature corresponding to the quasi-2D ($n$ = 2) components. (B) The kinetics of the low-energy feature (inverse Hilbert transform) corresponding to the 3D perovskites. (C) TCSPC of the neoPACl-passivated sample at 580 nm.

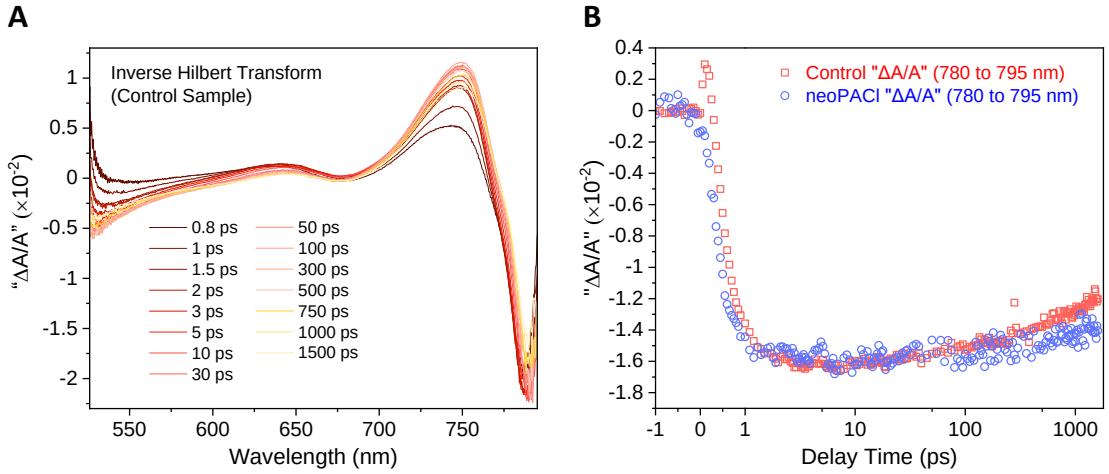


**Figure S15.** (A) Inverse Hilbert transform of the TR spectra of control sample pumped at 520-nm. (B) The kinetics of the low-energy feature (inverse Hilbert transform) corresponding to the control and neoPACl-passivated perovskite films.

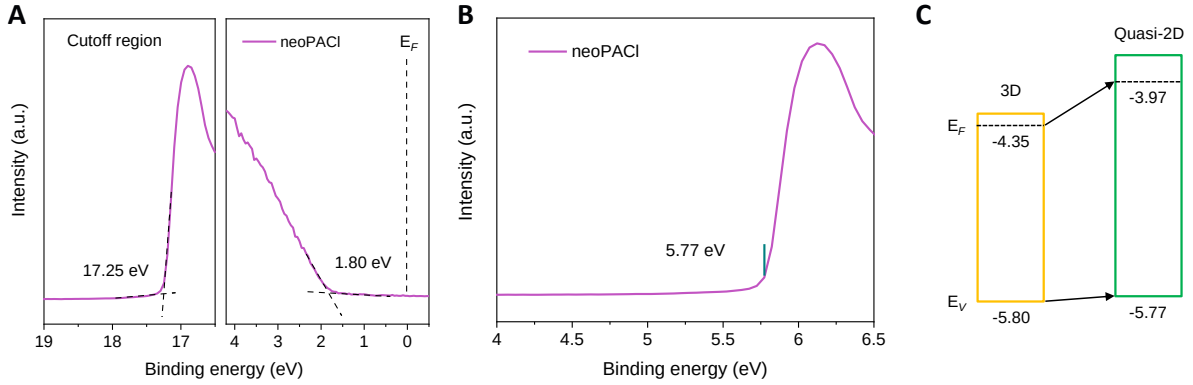


**Figure S16.** UPS spectra ($hv$ = 21.22 eV) of the secondary electron cutoff (A) and the valence band maximum of neoPACl-perovskite films (B). (C) Schematic energy level of the pristine[7] and quasi-2D terminated films.

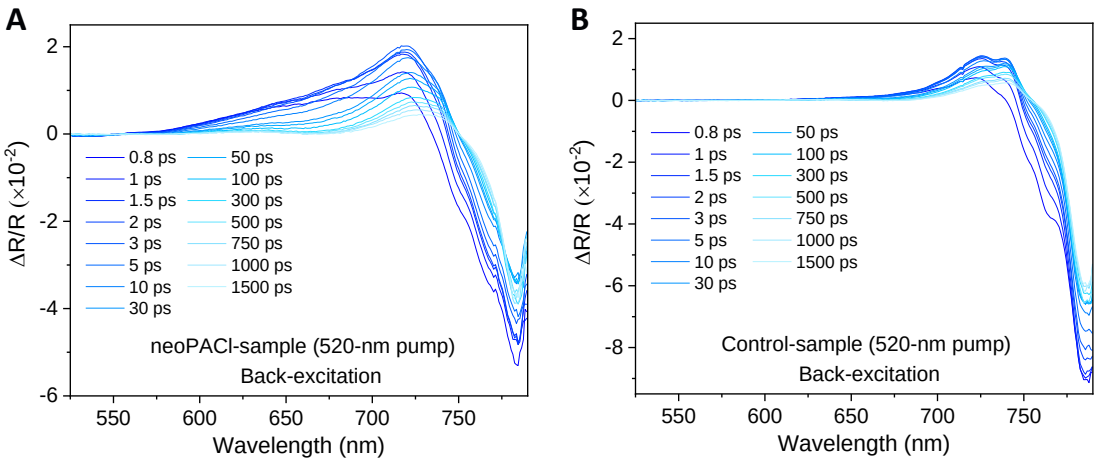


**Figure S17.** Transient reflection spectra under 520-nm pump from the back for (A) a neoPACl-passivated sample and (B) a pure 3D sample.

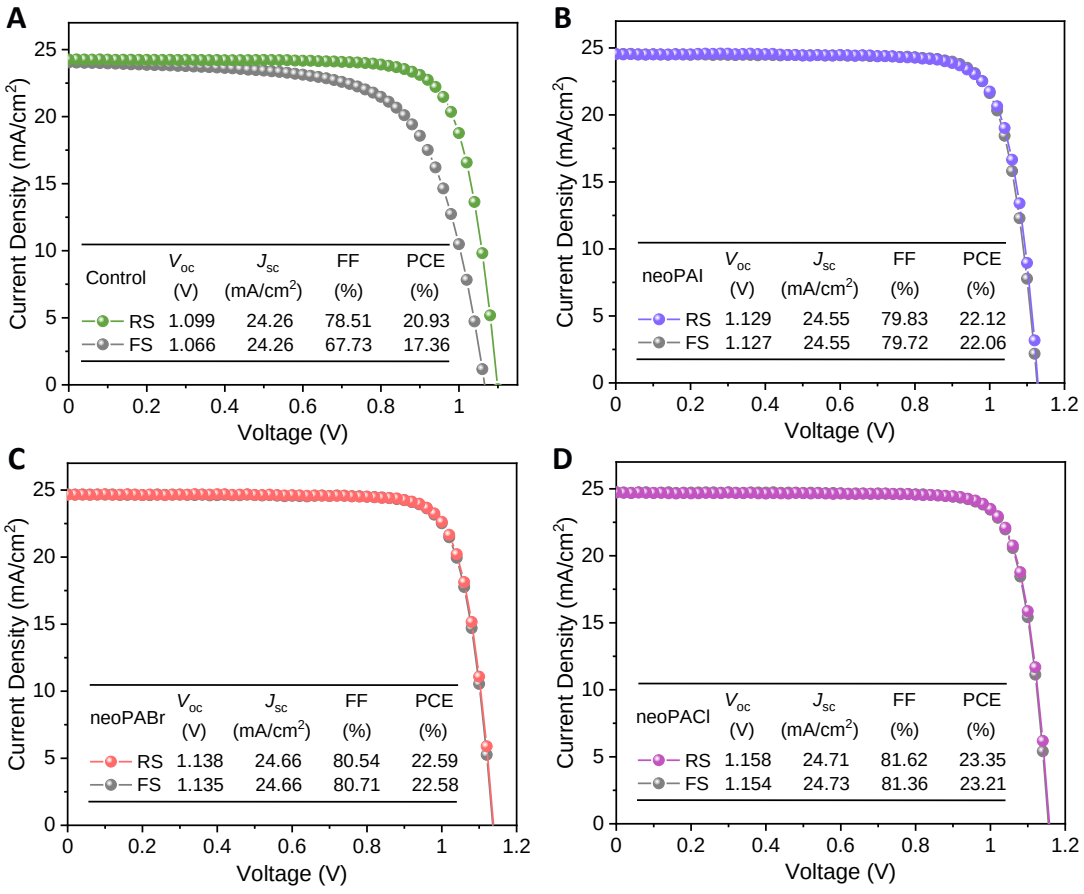


**Figure S18.** *J*–*V* curves of the champion devices with different treatment in comparison to the control obtained from reverse and forward scans under AM 1.5G illumination at 100 mW cm$^{-2}$.

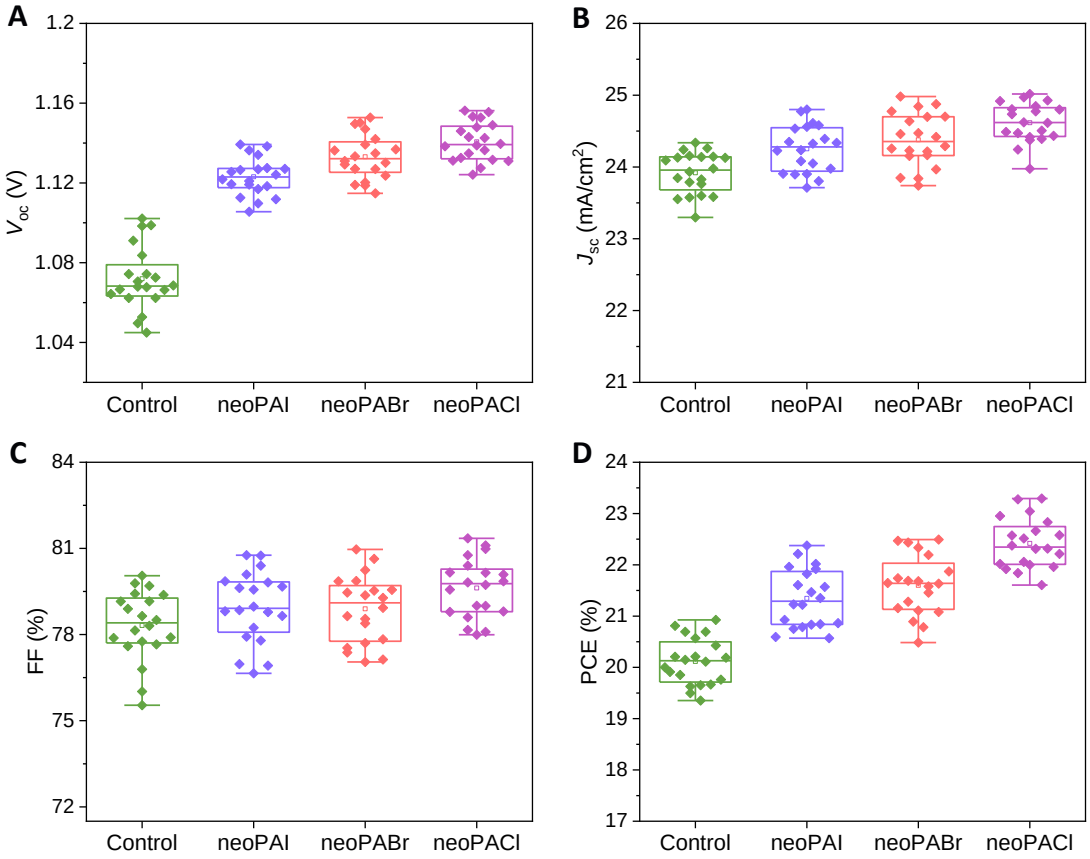


**Figure S19.** $V_{oc}$ (A), $J_{sc}$ (B), FF (C), and PCE (D) statistics of 20 devices with different treatments in comparison to the control. Error bars indicate the minimum and maximum values, and the middle square in each box represents the median value.

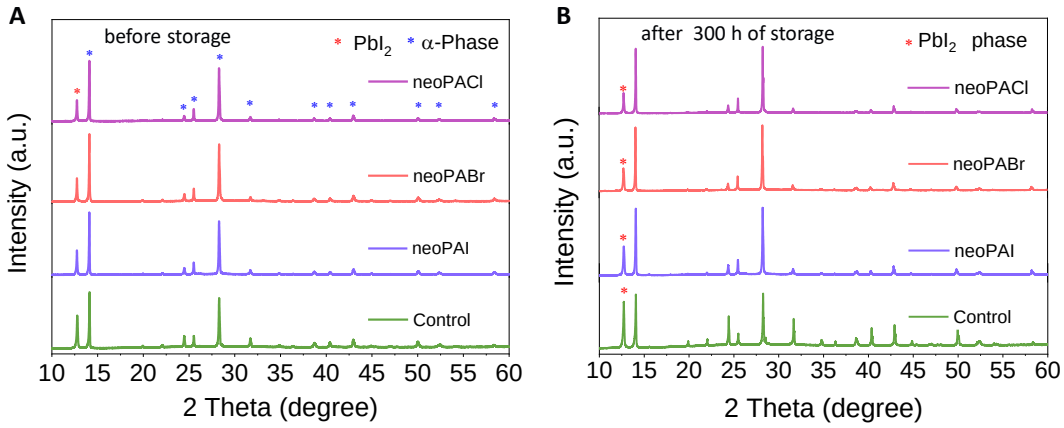


**Figure S20.** Comparison XRD patterns of the perovskite films based on neoPAX passivation with control film before and after 300 h storage in the atmosphere (20%RH).

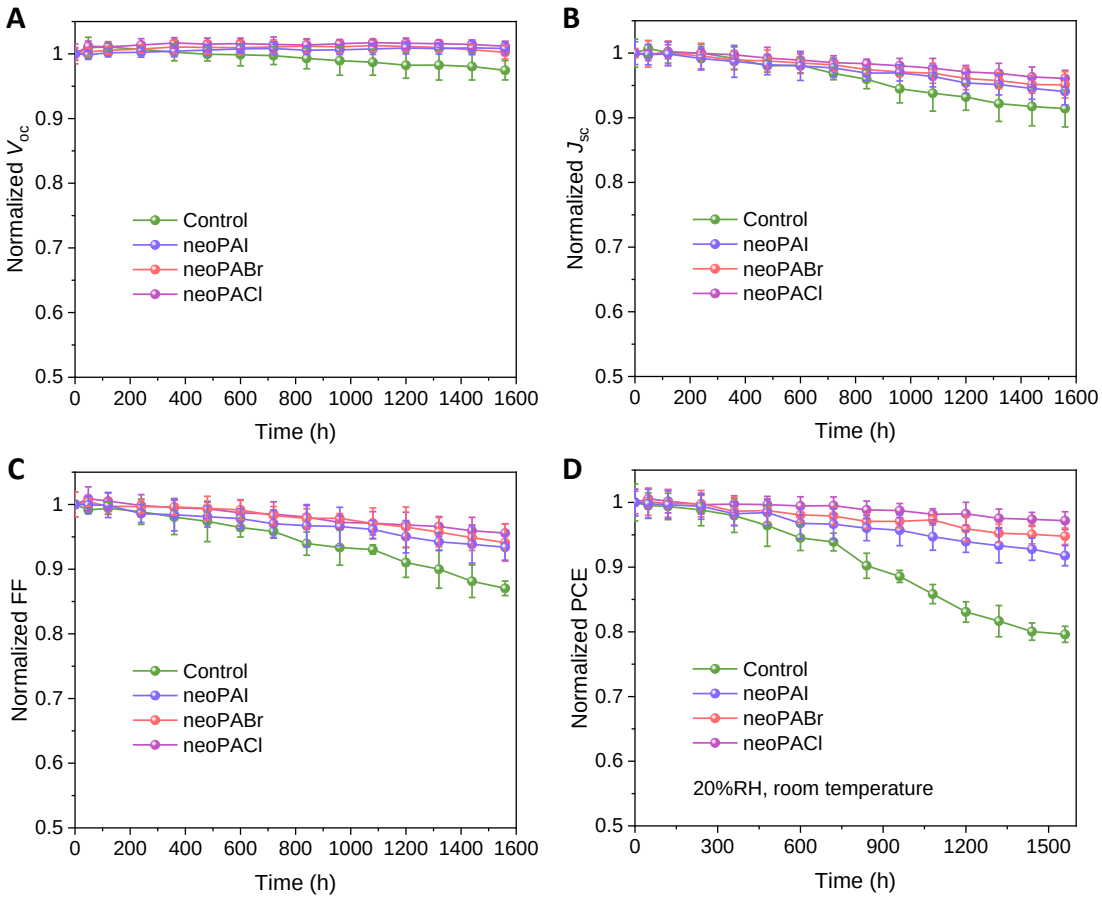


**Figure S21.** Long-term stability results without encapsulation under ambient conditions with a relative humidity about 20% for PSCs without and with neoPAI, neoPABr and neoPACl passivation.

**Table S1.** Carrier lifetime for perovskite films without and with post-treatment. The TRPL curves are fitted according to the formula $y = A_1\exp(-\tau/\tau_1) + A_2\exp(-\tau/\tau_2)$. Carrier lifetimes are calculated by the formula: $\tau_{ave} = (\sum A_i\tau_i^2) / (\sum A_i\tau_i)$.

| Sample | $A_1$ | $\tau_1$ (ns) | $A_2$ | $\tau_2$ (ns) | $\tau_{ave}$ (ns) |
|---|---|---|---|---|---|
| Control | 0.71±0.01 | 65.06±0.01 | 0.02±0.01 | 183.75±0.01 | 110.30±0.01 |
| neoPAI | 0.30±0.01 | 24.25±0.01 | 0.08±0.01 | 435.54±0.01 | 365.32±0.01 |
| neoPABr | 0.35±0.01 | 73.64±0.01 | 0.11±0.01 | 417.71±0.01 | 295.06±0.01 |
| neoPACl | 0.53±0.01 | 24.09±0.01 | 0.13±0.01 | 780.03±0.01 | 692.83±0.01 |

**Table S2.** Comparison of the photovoltaics parameters for the perovskite solar cells without and with different concentration of neoPAX under the reverse scan (1.2 to −0.2 V).

| | Concentration | $V_{oc}$ (V) | $J_{sc}$ (mA cm$^{-2}$) | FF | PCE (%) |
|---|---|---|---|---|---|
| Control | - | 1.076±0.023 | 24.23±0.43 | 0.78±0.02 | 20.27±0.51 |
| neoPAI | 10 mM | 1.096±0.016 | 24.31±0.48 | 0.79±0.02 | 21.06±0.31 |
| | 15 mM | 1.109±0.007 | 24.39±0.36 | 0.80±0.01 | 21.58±0.57 |
| | 20 mM | 1.123±0.017 | 24.33±0.58 | 0.79±0.02 | 21.50±0.55 |

| | | | | | |
|---|---|---|---|---|---|
| | 25 mM | 1.122±0.011 | 24.52±0.21 | 0.79±0.02 | 21.76±0.44 |
| | 30 mM | 1.131±0.008 | 24.47±0.32 | 0.78±0.01 | 21.47±0.62 |
| | 40 mM | 1.130±0.007 | 23.46±0.71 | 0.75±0.02 | 20.07±0.33 |
| neoPABr | 10 mM | 1.090±0.016 | 24.62±0.30 | 0.79±0.02 | 21.03±0.33 |
| | 15 mM | 1.112±0.012 | 24.65±0.27 | 0.78±0.02 | 21.46±0.76 |
| | 20 mM | 1.129±0.009 | 24.67±0.31 | 0.78±0.02 | 21.67±0.85 |
| | 25 mM | 1.135±0.005 | 24.63±0.48 | 0.79±0.01 | 22.02±0.37 |
| | 30 mM | 1.133±0.006 | 24.14±0.40 | 0.77±0.02 | 21.18±0.45 |
| | 40 mM | 1.143±0.013 | 23.02±0.87 | 0.76±0.02 | 20.14±0.88 |
| neoPACl | 10 mM | 1.094±0.017 | 24.68±0.21 | 0.79±0.01 | 21.47±0.32 |
| | 15 mM | 1.114±0.009 | 24.73±0.29 | 0.80±0.01 | 22.08±0.28 |
| | 20 mM | 1.125±0.009 | 24.75±0.27 | 0.80±0.01 | 22.27±0.51 |
| | 25 mM | 1.146±0.008 | 24.76±0.31 | 0.81±0.01 | 22.68±0.59 |
| | 30 mM | 1.147±0.010 | 24.28±0.49 | 0.79±0.01 | 21.88±0.60 |
| | 40 mM | 1.146±0.007 | 23.71±0.73 | 0.76±0.02 | 20.69±0.87 |

**Table S3.** Comparison of some representative reported literature on 2D/3D perovskite solar cells based on n-i-p structure.

| 2D phase | Device configuration | PCE (%) | Ref. |
|---|---|---|---|
| $MA_3Bi_2I_9$ | FTO/compact-$TiO_2$/$MAPbI_3$/Spiro-OMeTAD/Au | 18.97 | [8] |
| $IBA_2FAPb_2I_7$ | FTO/compact-$TiO_2$/ meso-$TiO_2$/$FAPbI_3$/2D/Spiro-OMeTAD/Au | 22.7 | [9] |
| $(DIAC)_2PbI_4$ | FTO/compact-$TiO_2$/meso-$TiO_2$/PMMA:PCBM/DIAC/$Cs_{0.07}Rb_{0.03}FA_{0.765}MA_{0.135}PbI_{2.55}Br_{0.45}$/DIAC/Spiro-OMeTAD/Au | 23.27 | [10] |
| $BAI_2FAPb_2I_7$ | FTO/meso-$TiO_2$/$Cs_{0.05}FA_{0.79}MA_{0.16}PbI_{2.49}Br_{0.51}$/2D/Spiro-OMeTAD/Au | 21.1 | [11] |
| $(PEA)_2FAPb_2I_7$ | FTO/c-$TiO_2$/$FAPbI_3$/2D/Spiro-OMeTAD/Au | 21.15 | [12] |
| $(2\text{-}TMABr)_2FA_{n-1}PbI_{3n+1}$ | FTO/compact-$TiO_2$/meso-$TiO_2$/$[(FAPbI_3)_{0.87}(MAPbBr_3)_{0.13}]_{0.92}(CsPbI_3)_{0.08}$/2D/Spiro-OMeTAD/Au | 20.82 | [13] |
| $(OAI)_2FA_{n-1}PbI_{3n+1}$ | FTO/compact-$TiO_2$/ns-$TiO_2$/$(FAPbI_3)_{0.95}(MAPbBr_3)_{0.05}$/2D/Spiro-OMeTAD/Au | 23.31 | [14] |
| $(FEA)_2PbI_4$ | FTO/c-$TiO_2$/meso-$TiO_2$/$Cs_{0.04}MA_{0.04}FA_{0.92}PbI_3$/2D/Spiro-OMeTAD/Au | 22.16 | [15] |
| $EDBEPbI_4$ | FTO/$SnO_2$/$Cs_{0.05}(FA_{0.83}MA_{0.17})_{0.95}Pb(I_{0.83}Br_{0.17})_3$/2D/SpiroOMeTAD/Au | 21.06 | [16] |
| $(HTAB)_2FAn\text{-}1PbI_{3n+1}$ | FTO/c-$TiO_2$/meso-$TiO_2$/$FAPbI_3)_{0.95}(MAPbBr_3)_{0.05}$/2D/P3HT/Au | 23.3 | [17] |
| $(neoPA)_2(FA)_{(n-1)}Pb_nI_{(3n+1)}$ | ITO/$SnO_2$/$FA_{1-x}MA_xPbI_3$/2D/Spiro-OMeTAD/Au | 23.35 | This work |

Supplementary Reference

[1] I. W. H. Oswald, A. A. Koegel, J. R. Neilson, *Chem. Mat.* **2018**, 30, 8606.
[2] C. C. Stoumpos, C. D. Malliakas, M. G. Kanatzidis, *Inorg. Chem.* **2013**, 52, 9019.
[3] B. L. Henke, E. M. Gullikson, J. C. Davis, *Atom. Data Nucl. Data Tables* **1993**, 55, 349.
[4] C. Lermer, S. T. Birkhold, I. L. Moudrakovski, P. Mayer, L. M. Schoop, L. Schmidt-Mende, B. V. Lotsch, *Chem. Mat.* **2016**, 28, 6560; H. Chen, J. Lin, J. Kang, Q. Kong, D. Lu, J. Kang, M. L. Lai, L. N. Quan, Z. N. Lin, J. B. Jin, L. W. Wang, M. F. Toney, P. D. Yang, *Sci. Adv.* **2020**, 6, 8.
[5] Z. X. Wang, W. Q. Liao, H. Y. Ye, Y. Zhang, *Dalton Trans.* **2015**, 44, 20406.
[6] J. Hidalgo, C. A. R. Perini, A. F. Castro-Mendez, D. Jones, H. Kobler, B. Lai, R. P. Li, S. J. Sun, A. Abate, J. P. Correa-Baena, *ACS Energy Lett.* **2020**, 5, 3526; G. K. Williamson, W. H. Hall, *Acta Metallurgica* **1953**, 1, 22.
[7] Q. Jiang, Z. Y. Ni, G. Y. Xu, Y. Lin, P. N. Rudd, R. M. Xue, Y. W. Li, Y. F. Li, Y. L. Gao, J. S. Huang, *Adv. Mater.* **2020**, 32, 10.
[8] Y. Hu, T. Qiu, F. Bai, W. Ruan, S. Zhang, *Advanced Energy Materials* **2018**, 8.
[9] Y. Liu, S. Akin, A. Hinderhofer, F. T. Eickemeyer, H. Zhu, J. Y. Seo, J. Zhang, F. Schreiber, H. Zhang, S. M. Zakeeruddin, A. Hagfeldt, M. I. Dar, M. Gratzel, *Angew Chem Int Ed Engl* **2020**, 59, 15688.
[10] M. A. Mahmud, T. Duong, Y. Yin, J. Peng, Y. Wu, T. Lu, H. T. Pham, H. Shen, D. Walter, H. T. Nguyen, N. Mozaffari, G. D. Tabi, Y. Liu, G. Andersson, K. R. Catchpole, K. J. Weber, T. P. White, *Small* **2020**, e2005022.
[11] C. Liu, J. Sun, W. L. Tan, J. Lu, T. R. Gengenbach, C. R. McNeill, Z. Ge, Y. B. Cheng, U. Bach, *Nano letters* **2020**, 20, 1240.
[12] T. Niu, J. Lu, X. Jia, Z. Xu, M. C. Tang, D. Barrit, N. Yuan, J. Ding, X. Zhang, Y. Fan, T. Luo, Y. Zhang, D. M. Smilgies, Z. Liu, A. Amassian, S. Jin, K. Zhao, S. Liu, *Nano letters* **2019**, 19, 7181.
[13] A. A. Sutanto, P. Caprioglio, N. Drigo, Y. J. Hofstetter, I. Garcia-Benito, V. I. E. Queloz, D. Neher, M. K. Nazeeruddin, M. Stolterfoht, Y. Vaynzof, G. Grancini, *Chem* **2021**, 7, 1903.
[14] H. Kim, S. U. Lee, D. Y. Lee, M. J. Paik, H. Na, J. Lee, S. I. Seok, *Advanced Energy Materials* **2019**, 9, 1902740.
[15] Y. H. Liu, S. Akin, L. F. Pan, R. Uchida, N. Arora, J. V. Milic, A. Hinderhofer, F. Schreiber, A. R. Uhl, S. M. Zakeeruddin, A. Hagfeldt, M. I. Dar, M. Gratzel, *Science Advances* **2019**, 5.
[16] P. Li, Y. Zhang, C. Liang, G. Xing, X. Liu, F. Li, X. Liu, X. Hu, G. Shao, Y. Song, *Advanced materials* **2018**, 30, e1805323.
[17] E. H. Jung, N. J. Jeon, E. Y. Park, C. S. Moon, T. J. Shin, T. Y. Yang, J. H. Noh, J. Seo, *Nature* **2019**, 567, 511.